Image transfer with subwavelength resolution to metal–dielectric interface

Varat Intaraprasonk,[1] Zongfu Yu,[2] and Shanhui Fan[2,*]

[1]*Department of Applied Physics, Stanford University, Stanford, California 94305, USA*
[2]*Department of Electrical Engineering, Stanford University, Stanford, California 94305, USA*
**Corresponding author: shanhui@stanford.edu*

Received October 19, 2010; revised February 3, 2011; accepted March 2, 2011;
posted March 8, 2011 (Doc. ID 136655); published April 29, 2011

In image transfer, one aims to reproduce at an image plane the field distribution of the field at the source plane. We consider a near-field image transfer scheme where an image with subwavelength resolution can be transferred to a metal–dielectric interface. In this scheme, the presence of a surface plasmon polariton provides a large wave vector range where the transfer function is flat, thus enabling the image transfer with subwavelength resolution.

OCIS codes: 070.7345, 240.0240.

In image transfer, one aims to reproduce at an image plane ($z = d$) the field distribution of the field at the source plane ($z = 0$). In the far field, the smallest feature size that can be transferred is of the order of the wavelength of the light (λ), because only the propagating wave vector components contribute. These propagating components, after travelling for a distance, will acquire a phase shift that can be compensated with a lens. On the other hand, the fast-varying spatial information, contained in the evanescent wave vector components, decays exponentially in the propagating direction and does not contribute when the distance is large enough. The problem of evanescent decay is less severe in the near-field regime ($d \le \lambda$). Moreover, in the near-field regime, it has been shown that a "super lens," with a negative-index or negative-dielectric material [1–5], can be used to amplify the evanescent components and achieve image transfer from the source plane to the image plane with subwavelength resolution. One of the problems with the super lens is that the wave has to go through a slab of the negative-index or negative-dielectric material, where there is significant loss.

Here we considered another proposed scheme, where negative-dielectric material such as a plasmonic metal is placed after the image plane and the evanescent components are amplified by the reflection from the negative-dielectric material [Fig. 1(a)]. Comprehensive theoretical analyses of this scheme have been done [6–8], where both the global contrast (in terms of intensity in the entire region between the source and the negative-dielectric medium) and local contrast (in terms of lateral contrast in one slice at the image plane), have been considered.

Building upon these previous works, in this paper, we specifically consider the possibility of image transfer to the metal–air interface, shown in Fig. 1(a), where the evanescent enhancement effect is expected to be the greatest. In this case, the performance of this scheme can be easily understood in terms of a transfer function in momentum space. In particular, we show that subwavelength image transfer can occur when the transfer function is relatively flat over a large range of wave vector space. We introduce a quantitative measure of flatness of the transfer function. We also provide direct numerical evidence that this scheme can operate in the ultraviolet wavelength ranges with realistic material loss.

To mathematically describe image transfer for the system shown in Fig. 1, as a simple example we consider the two-dimensional case and define the transfer function $T(k_y)$ (following [9,10]) by

$$F_t(k_y, z = d) = F_i(k_y, z = 0)T(k_y), \tag{1}$$

where $F_i(k_y, z = 0)$ is the Fourier transform of $F_i(y, z = 0)$, the *incident* field distribution at the initial plane ($z = 0$), and $F_t(k_y, z = d)$ is the Fourier transform of $F_t(y, z = d)$, the *total* field distribution at the image plane ($z = d$). In order to achieve image transfer, our aim is to create a transfer function that is "flat," meaning that it remains nearly constant across large range of k_y.

To show that flat transfer function is useful for image transfer and to quantify the flatness of a transfer function, we measure how much such a transfer function deviates from the ideal one. The ideal transfer function for the purpose of image transfer is a constant valued function in k_y so that all k_y components are transferred equally. This means its inverse Fourier transform $\tilde{T}(y)$ [the point spread function (PSF)] is a delta function. One way to measure the deviation from this delta function PSF is then to measure its second moment $\int y^2 |\tilde{T}(y)|^2 \mathrm{d}y$ (for an example, see [11]). By normalizing the transfer function (because an overall constant does not affect image transfer), normalizing the length scale to wavelength (λ) to get a dimensionless number, and using Parseval's theorem, we get

$$\left(\frac{2\pi}{\lambda}\right)^2 \frac{\int_{-\infty}^{\infty} y^2 |\tilde{T}(y)|^2 \mathrm{d}y}{\int_{-\infty}^{\infty} |\tilde{T}(y)|^2 \mathrm{d}y} = k_0^2 \frac{\int_{-\infty}^{\infty} |\mathrm{F.T.}[y\tilde{T}(y)]|^2 \mathrm{d}k_y}{\int_{-\infty}^{\infty} |\mathrm{F.T.}[\tilde{T}(y)]|^2 \mathrm{d}k_y} = k_0^2 \frac{\int_{-\infty}^{\infty} \left|\frac{d}{dk_y}[T(k_y)]\right|^2 \mathrm{d}k_y}{\int_{-\infty}^{\infty} |T(k_y)|^2 \mathrm{d}k_y} \equiv N_f, \tag{2}$$

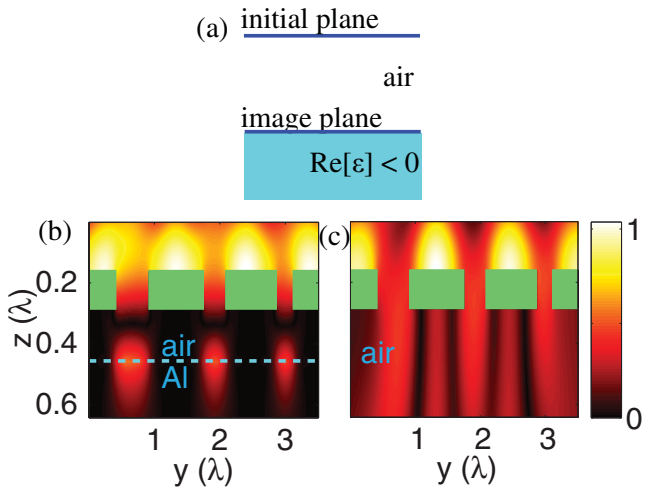

Fig. 1. (Color online) (a) Schematic of the near-field image transfer to the metal–dielectric interface. (b) FDFD simulation of the scheme. A plane wave at $\lambda = 116\,\mathrm{nm}$, at which $\epsilon_{\mathrm{Al}} = -1.047 + 0.077i$, is incident from the top, through a mask structure consisting of air slits in a metal film. (Metal mask is shown as green). The slit widths are $\lambda/2$, $\lambda/3$, and $\lambda/4$, respectively. (c) Same setup as (b) but without Al. In (b) and (c), the color maps the absolute value of the field amplitude.

where F.T.[...] denotes Fourier transform, and $k_0 = 2\pi/\lambda$. Thus, we can define a measure of the flatness of the transfer function N_f as in Eq. (2), which involves the integral of the magnitude of the slope of the transfer function. Lower N_f represents a flatter transfer function in wave vector space, and it results in a better image since the PSF is narrower in real space.

In the structure shown in Fig. 1(a), the transfer occurs through a dielectric with a positive dielectric constant ϵ_d. In such a dielectric,

$$\left(\frac{\partial^2}{\partial y^2} + \frac{\partial^2}{\partial z^2} + k_d^2\right) F = 0, \tag{3}$$

where $k_d^2 = \epsilon_d(\omega/c)^2$, ω is the angular frequency, and c is the speed of light. This equation describes the propagation of the field F, and, along with Eq. (1), gives the free space transfer function T_f for the dielectric

$$T_f(k_y, z) = \exp(ik_{z,d}(k_y)z), \tag{4}$$

where $k_{z,d} = (k_d^2 - k_y^2)^{1/2}$. For evanescent components $k_y > k_d$, T_f decays exponentially in z. Perhaps more importantly, for image transfer purposes, we note that T_f is also approximately an exponential decay function in k_y, meaning that the different Fourier components in the initial field will decay at significantly different rates, giving a large distortion in the image plane.

Here we show that the evanescent amplification scheme, commonly used for compensating exponential decay in z [1–5], can also be designed to generate a relatively flat transfer function in k_y space. As a demonstration, we put a material with negative permittivity $\epsilon_m < 0$ in the region $z > d$, where $z = d$ is the image plane [Fig. 1(a)], and consider the TM polarization by setting the field F to be the magnetic field along the x direction. The transfer function is then

$$T(k_y) = (1 + r(k_y))\exp(ik_{z,d}d). \tag{5}$$

Here $r(k_y)$ is the reflection coefficient at the interface, and has the form

$$r(k_y) = \left(\frac{k_{z,d}}{\epsilon_d} - \frac{k_{z,m}}{\epsilon_m}\right) \Big/ \left(\frac{k_{z,d}}{\epsilon_d} + \frac{k_{z,m}}{\epsilon_m}\right), \tag{6}$$

where $k_{z,m} = (\epsilon_m(\omega/c)^2 - k_y^2)^{1/2}$. For propagating components (real $k_{z,d}$), the negative-dielectric material essentially behaves as a good mirror; hence $|r(k_y)| \approx 1$. For evanescent components (imaginary $k_{z,d}$), $r(k_y)$ is large when $k_{z,d}/\epsilon_d \approx -k_{z,m}/\epsilon_m$, which occurs when the parallel wave vector $k_y \approx k_{\mathrm{SP}}$ where

$$k_{\mathrm{SP}} = \mathrm{Re}\left[(\omega/c)\sqrt{\frac{\epsilon_m\epsilon_d}{\epsilon_m + \epsilon_d}}\right] \tag{7}$$

is the wave vector of the propagating surface polariton wave at the interface.

As an illustration, we consider the case of an interface between air ($\epsilon_d = 1$) and aluminum (Al). Figure 2(a) shows the dispersion relation of the surface polariton at the interface between air ($\epsilon_d = 1$) and Al, for the lossless case (dashed curve) and realistically lossy case (solid curve). The values of the permittivity of Al as a function of frequency are taken from [12]. At the frequency of $\omega = 1.63 \times 10^{16}\,\mathrm{rad/s}$ ($\lambda = 116\,\mathrm{nm}$), ($\epsilon_m = -1.047$, $k_{\mathrm{SP}} = 4.7k_d$) we plot in Fig. 2(b) for the lossless case the transfer function $T(k_y, d)$ at three different image distances d. (We choose this frequency so that ϵ_m is close to -1 and k_{SP} is large.) The transfer function indeed diverges at k_{SP}. In Fig. 2(c), we show a similar plot with loss included at the same frequency ($\omega = 1.63 \times 10^{16}\,\mathrm{rad/s}$, $\epsilon_m = -1.047 + 0.077i$). The main features are similar, with maximum of $|T|$ occurring around k_{SP} for each case. The position of such

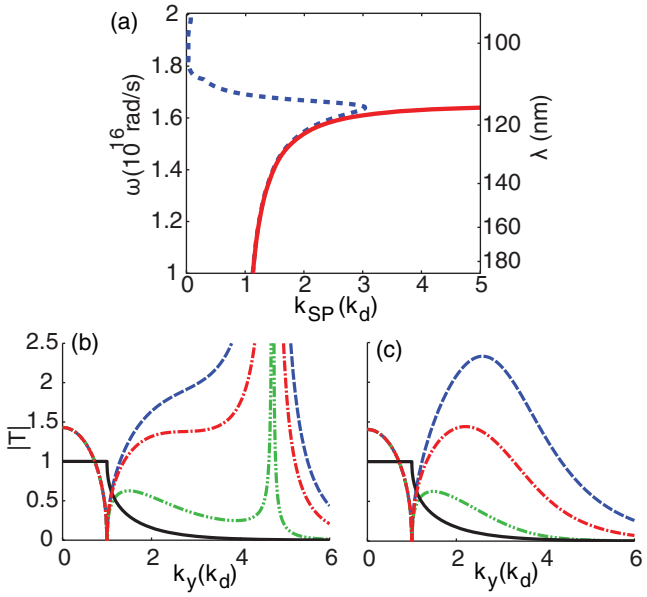

Fig. 2. (Color online) (a) Dispersion curve of the surface plasmon between Al and air for lossless case (solid curve) and lossy case (dashed curve). (b) Transfer functions for the air–Al system at different image transfer distances (d); dashed, $d = 0.15\lambda$; dotted–dashed, $d = 0.17\lambda$; dotted–dotted–dashed, $d = 0.25\lambda$. The solid curve is the transfer function without Al. (c) Same as (b) but for lossy case; dashed, $d = 0.125\lambda$, $N_f = 0.83$; dotted–dashed, $d = 0.16\lambda$, $N_f = 1.4$; dotted–dotted–dashed, $d = 0.25\lambda$, $N_f = 2.9$.

maxima moves to lower k_y with increasing d due to the evanescent decay. In both cases, the transfer function now has significant amplitude in the evanescent region. More importantly, it is relatively flat in k_y, in the sense that the low- and high-spatial frequency components have more similar transfer function coefficients than typical near-field systems. Such a flat function is desirable for image transfer of a wide range of feature sizes.

We now provide a direct numerical confirmation of our image transfer scheme using the finite-difference frequency-domain (FDFD) simulation [13] [Fig. 1(b)]. The source is set up by having a plane wave from the top incident on the holes in the mask modeled as perfect conductor (green rectangles). The widths of the holes are $\lambda/2$, $\lambda/3$ and $\lambda/4$. Based on our discussion above, we have chosen $\omega = 1.63 \times 10^{16}$ rad/s. The object plane (the bottom interface of the mask) is placed at a transfer distance $d = 0.16\lambda$ from the Al ($\epsilon_m = -1.047 + 0.077i$). The image plane is the front interface of Al. We can see that the field at the image plane closely resembles the profile of the incident plane. For comparison, the simulation result of the same setup but without Al is shown in Fig. 1(c), where significant distortion is seen at the image plane. Note that, in this setup, the transfer function from Eq. (5) may require a correction from the back reflection from the mask [14]. However, the full field simulation still demonstrates subwavelength image transfer.

To estimate the smallest feature size $w_{\min}$ that can be transferred with our scheme, we use the fact that the transfer function has significant amplitude at least up to $k_y = k_{\mathrm{SP}}$. Therefore,

$$w_{\min} \lesssim 2\pi/k_{\mathrm{SP}}. \tag{8}$$

For example, in Fig. 2(a), we can see k_{SP} at our operating frequency is $3k_d$, so we can transfer the step function with the width as narrow as $\lambda/3$ to $\lambda/4$ in Fig. 1(b), in consistency with the simulation.

Next, we compare our image transfer scheme to the super lens proposed in [1]. In one of the super lens schemes, a slab of negative permittivity material is placed between the object plane and the image plane [as in Fig. 3(b)]. The wave goes through the lossy material in the super lens scheme, while it only goes through air gap in our scheme. Therefore, our scheme should be less susceptible to material loss, meaning the peak height should not change much with the increase in loss. This is confirmed in Fig. 3 where we plot the transfer functions of the two schemes with the same total air gap distances ($d = 0.16\lambda$) and $\epsilon_m = -1 + i\epsilon_m''$ for several values of ϵ_m''. N_f is given on the plot. We can also see that, even though the super lens gives a higher transfer function for evanescent components, its high and sharp peak and the discrepancy between the propagating and evanescent transfer function lead to higher N_f. Therefore, in terms of the spatial extent of the PSF, our image transfer scheme is superior to that of the super lens.

For experimental implementation and potential lithographic application of our scheme, it is important to discuss image transfer in a multilayer system. (The experiment for the negative-index super lens [2,3], for example, involves the use of a photoresist layer.) As an illustration, we consider a system at $\omega = 1.24 \times 10^{16}$ rad/s ($\lambda = 152$ nm) consisting of an air gap ($\epsilon = 1$, thickness $= 0.15\lambda$) and a photoresist (PR) layer ($\epsilon = 2.7$, thickness $= 0.05\lambda$) that is on top of an Al ($\epsilon = -2.6 + 0.22i$) region, as shown in Fig. 4(a). (We choose this frequency so that $\epsilon_m \approx -\epsilon_{\mathrm{PR}}$.) The corresponding transfer function from a source plane located in air at $z = 0$ to the PR–Al interface [$T(k_y, z = 0.21\lambda)$] is calculated using a transfer matrix and is shown in Fig. 4(b). We see that the transfer function can be made flat even in the presence of the PR layer. The FDFD simulation with the same mask as Figs. 1(b) and 1(c) is shown in Fig. 4(c), using a realistic dielectric constant for chromium mask ($\epsilon = -0.55 + 1.43i$). We can see that the image field also closely resembles the profile of the mask. Note that, because of the high field confinement in the z direction at the PR–Al interface, the behavior of this three-layer system is primarily determined by the surface plasmon at the PR–Al interface [15].

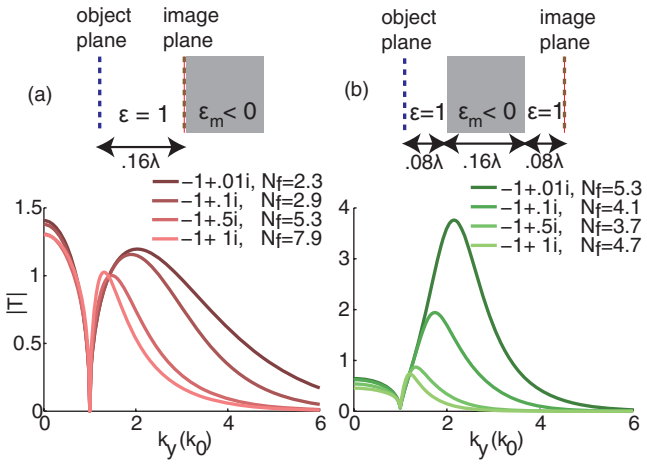

Fig. 3. (Color online) Transfer functions for several values of ϵ_m for (a) our scheme with image plane at the front interface of the negative permittivity material, and for (b) the negative permittivity super lens scheme in [1]. The first numbers in the legend are ϵ_m.

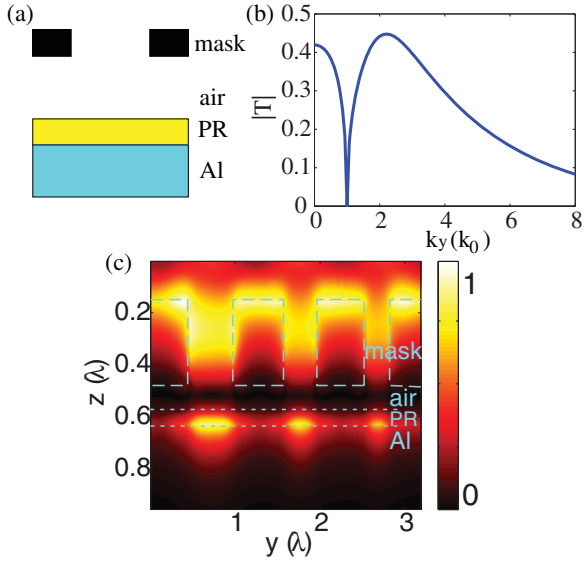

Fig. 4. (Color online) (a) Schematic for the image transfer with extra PR layer. (b) Transfer function for the setup in (a) with $\lambda = 152$ nm, $\epsilon_{\mathrm{PR}} = 2.7$, $\epsilon_{\mathrm{Al}} = -2.6 + 0.22i$. Thickness of the air gap and the PR layer are 0.15λ and 0.05λ, respectively. (c) FDFD simulation of the setup in (b) with the same mask dimension as Figs. 1(b) and 1(c) but with a realistic dielectric constant ($\epsilon_{\mathrm{mask}} = -0.55 + 1.43i$).

As final remarks, in previous works [6–8,16–18], a mask layer was put directly on top of a PR layer, and the PR layer can be put on additional metal layer. The image formation was assisted by surface plasmons on either the mask, or the additional metal layer, or both. In contrast to all these works [6–8,16–18], we consider here a noncontact scheme where there is an air gap between the mask and the PR. In addition, the maximal of the field is on the image plane, away from the mask. Both aspects may be attractive for practical considerations. For example, having a noncontact scheme is essential in some of the recent experimental demonstrations of a fling plasmonic lens in near-field nanolithography [19]. Also, while we have considered a very simple mask design, more complex masks (e.g., a phase mask) can be used to improve the contrast at the image plane. Finally, we note that what gives rise to the evanescent amplification is the presence of a surface state. Thus, instead of using the negative permittivity material, one can use other means such as metamaterial to generate surface states [20,21] if there is a need to operate in other frequencies such as infrared.

ACKNOWLEDGMENTS

Varat Intaraprasonk is supported by a Stanford Graduate Fellowship.

REFERENCES

1. J. B. Pendry, "Negative refraction makes a perfect lens," Phys. Rev. Lett. **85**, 3966–3969 (2000).
2. N. Fang, H. Lee, C. Sun, and X. Zhang, "Sub-diffraction-limited optical imaging with a silver superlens," Science **308**, 534–537 (2005).
3. D. Melville, R. Blaikie, and C. Wolf, "Submicron imaging with a planar silver lens," Appl. Phys. Lett. **84**, 4403–4405 (2004).
4. R. Blaikie, M. Alkaisi, S. McNab, and D. Melville, "Nanoscale optical patterning using evanescent fields and surface plasmons," Int. J. Nanosci. **3**, 405–417 (2004).
5. T. Xu, L. Fang, J. Ma, B. Zeng, Y. Liu, J. Cui, C. Wang, Q. Feng, and X. Luo, "Localizing surface plasmons with a metal-cladding superlens for projecting deep-subwavelength patterns," Appl. Phys. B **97**, 175–179 (2009).
6. D. Shao and S. Chen, "Surface-plasmon-assisted nanoscale photolithography by polarized light," Appl. Phys. Lett. **86**, 253107 (2005).
7. D. Shao and S. Chen, "Numerical simulation of surface-plasmon-assisted nanolithography," Opt. Express **13**, 6964–6973 (2005).
8. M. Arnold and R. Blaikie, "Subwavelength optical imaging of evanescent fields using reflections from plasmonic slabs," Opt. Express **15**, 11542–11552 (2007).
9. R. Merlin, "Radiationless electromagnetic interference: evanescent-field lenses and perfect focusing," Science **317**, 927–929 (2007).
10. V. Intaraprasonk and S. Fan, "Wave-vector space picture for radiationless focusing and beaming," Opt. Lett. **34**, 2967–2969 (2009).
11. R. Muller and A. Buffington, "Real-time correction of atmospherically degraded telescope images through image sharpening," J. Opt. Soc. Am. **64**, 1200–1210 (1974).
12. E. D. Palik, ed., *Handbook of Optical Constants of Solids* (Academic, 1985).
13. G. Veronis, R. W. Dutton, and S. Fan, "Method for sensitivity analysis of photonic crystal devices," Opt. Lett. **29**, 2288–2290 (2004).
14. C. Moore, R. Blaikie, and M. Arnold, "An improved transfer-matrix model for optical superlenses," Opt. Express **17**, 14260–14269 (2009).
15. A. Karalis, E. Lidorikis, M. Ibanescu, J. D. Joannopoulos, and M. Soljacic, "Surface-plasmon-assisted guiding of broadband slow and subwavelength light in air," Phys. Rev. Lett. **95**, 063901 (2005).
16. Z. W. Liu, Q. H. Wei, and X. Zhang, "Surface plasmon interference nanolithography," Nano Lett. **5**, 957–961 (2005).
17. X. Luo and T. Ishihara, "Subwavelength photolithography based on surface-plasmon polariton resonance," Opt. Express **12**, 3055–3065 (2004).
18. X. Yang, L. Fang, B. Zeng, C. Wang, Q. Feng, and X. Luo, "Deep subwavelength photolithography based on surface plasmon polariton resonance with metallic grating waveguide heterostructure," J. Opt. **12**, 045001 (2010).
19. W. Srituravanich, L. Pan, Y. Wang, C. Sun, D. Bogy, and X. Zhang, "Flying plasmonic lens in the near field for high-speed nanolithography," Nat. Nanotechnol. **3**, 733–737 (2008).
20. J. B. Pendry, L. Martin-Moreno, and F. J. Garcia-Vidal, "Mimicking surface plasmons with structured surfaces," Science **305**, 847–848 (2004).
21. J. T. Shen, P. B. Catrysse, and S. Fan, "Mechanism for designing metallic metamaterials with a high index of refraction," Phys. Rev. Lett. **94**, 197401 (2005).